Instrumented Impact Testing of a Glass Swirl Mat-Reinforced Reaction Injection-Molded Polyamide Block Copolymer (NBC)

J. KARGER-KOCSIS

Institut für Verbundwerkstoffe GmbH, Universität Kaiserslautern, Pf.3049, D-6750 Kaiserslautern, Germany

SYNOPSIS

The fracture behavior of a reaction injection-molded (RIM) polyamide block copolymer (NBC) reinforced with a continuous glass strand mat (swirl mat) was studied in instrumented high-speed impact-bending tests. Investigations were carried out on Charpy and Izod specimens of different size and notching direction to elucidate specimens' size effects. From the tests performed at ambient temperature and −40°C, fracture mechanical parameters (fracture toughness, fracture energy) and E-modulus were derived. Changes observed in the above parameters of the matrix were attributed to a molding-induced skin-core morphology. Both fracture toughness and energy of the composites depended strongly on the type, i.e., on the ligament width (W) and length-to-span ratio (L_0/L) of the specimens. Reliable fracture mechanics data can be determined in three-point bending when $W > 12$ mm and $L_0/L > 1.7$ for the specimens. The fracture toughness and E-modulus increased monotonously, whereas the fracture energy reached a plateau as a function of fiber mat content. Their values were only slightly influenced by the temperature. It was also shown how molding- and machining-induced flaw size can be defined. The failure mode of the materials was studied by fractography and the failure events were summarized in a model and discussed.

INTRODUCTION

Reinforced reaction injection-molded (RRIM) polyamide-(PA) and polyurethane-based composites are promising candidates to replace metals in the automobile industry in the form of body panels, bumpers, and other exterior parts. The reaction injection-molded (RIM) technology allows a cost-effective production of large-area panels of sophisticated geometry that can hardly be achieved by injection molding or thermoforming of thermoplastic matrix composites. A further advantage of this technology is that the mechanical property profile of the resulting composite can be varied in a broad range by modification of the matrix (main-chain build-up, rubber modification of RIM PA-6[1] or by a proper selection of the reinforcements, e.g., milled glass fiber (GF) incorporated into the molten caprolactam, preplacement of continuous glass strand (swirl) mat, or woven GF fabrics into the mold[2] and the like. The automotive application of PA–RRIM (chopped fiber-reinforced composites) and –SRIM (from structural RIM involving continuous fiber-reinforced systems) necessitates their profound mechanical and, especially, impact characterization. On this topic, however, limited information is available in the literature.[2–5]

Presently, it seems that the largest parts with the required stiffness and toughness characteristics could be produced by use of GF mats preplaced into the mold. A preplaced GF mat-reinforced PA-6 prepared by *in situ* polymerization of caprolactam was the subject of an impact study carried out on an instrumented falling weight equipment at $v = 4$ m/s dart speed by Otaigbe and Harland.[3] The impact performance of the material in this study was interpreted by the concept of fracture mechanics, and fracture energy values were also reported.

Fracture mechanical data are of paramount im-

Journal of Applied Polymer Science, Vol. 45, 1595–1609 (1992)
 CCC 0021-8995/92/091595-15$04.00

portance since they can be treated as material-related properties. They are, however, completely lacking for composites with a nylon block copolymer (NBC) matrix. Determination of a fracture mechanics parameter for continuous GF strand mat-reinforced plastics may be associated with several problems[5]:

- Specimen size
  Machining of the specimens makes from the initial "continuous" reinforcement a "chopped" version, which may influence the fracture and failure processes.
- Anisotropy
  The fracture mechanical values may differ from each other depending on the notching and thus on impact direction. The scatter in the data should be related to the local arrangement of the mat[6] at the crack tip.
- Flaw-size effect
  It is widely accepted that the artificial notch should be corrected with the length of the processing or plastic zone to get reliable values for these materials (e.g., Ref. 3). The size of this zone, on the other hand, can hardly be determined, especially for materials that are opaque or in which fracture initiation is followed by a stable propagation stage instead of catastrophic failure.

This work is aimed at establishing dynamic fracture mechanical data for random or swirl GF mat-reinforced NBC–RIM composites at high-speed impact-bending loadings. It was intended further to contribute to the questions listed above by performing measurements on Izod and Charpy specimens of different size and notching direction. Finally, measurements were carried out also at low temperature ($T = -40°C$) in order to collect information about possible differences in the fracture and related failure phenomena.

EXPERIMENTAL

Materials

The plates investigated ($150 \times 150 \times 4$ mm^3) were molded by RAPRA Technology Ltd. (Shawbury, UK) using the components of the Nyrim 2000 system of DSM (Maastricht, The Netherlands). This NBC–RIM material of 1.14 g/cm^3 density was a block copolymer containing about 20 vol % elastomeric polyether soft segments. Based on gel permation chromatography using a Waters GPC device and a calibration for polystyrene, $M_n = 1.72 \times 10^4$ and $M_w = 3.58 \times 10^4$ g/mol were found in *m*-cresol at 90°C. According to differential scanning calorimetric (DSC) analysis, the NBC–RIM matrix exhibited $\approx$ 30% crystallinity, supposing 188.4 J/g melting enhalpy for the 100% crystalline PA-6.[7]

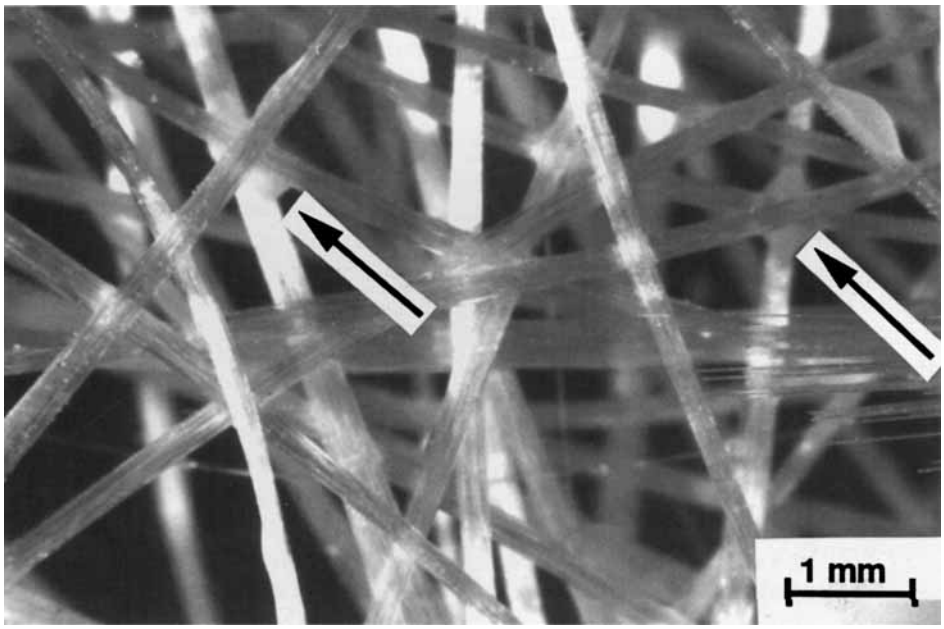

Figure 1 Macrophotograph taken on the continuous GF strand mat used. Arrows indicate for local bonding sites in the network structure of the mat.

Swirl GF mat loading ($\approx$ 20 to $\approx$ 50 wt %) were produced by stacking continuous E-glass strand mats (Unifilo U816 swirl mat from Vetrotex International, Aix-les-Bains, France) into the mold before filling up with the RIM components. This GF mat of 450 g/m^2 surface weight was sized by a silane compound and bonded by a polyester binder (Fig. 1). The strands with a diameter of about 150 μm were composed from GF monofilaments of 15 μm diameter and 25 tex strength. A NBC–SRIM composite, designated as "B," with $\approx$ 20 wt % reinforcement was molded by using a different GF strand mat (Unifilo U750). This GF mat possessed the same basic characteristics with the only exception that its strands were composed of both 25 and 50 tex strength filaments.

Specimens and Methods

Charpy and Izod specimens of different size and notching direction were sawed from the plaque according to Figure 2. Figure 2 indicates also the dimensions and designations of the specimens used. The dimensions of the Charpy (C–S, C–SN, C–B) and Izod (I) specimens followed the recommendations of the DIN 53 453 and ASTM D 256 standards, respectively. Controlled by a stereomicroscope, notching was performed by pressing a fresh razor blade into the specimen until the required depth. The razor blade was fixed in a supporting frame and mounted in a hand press that was loaded manually, i.e., without force or penetration rate control. This kind of notching did not produce observable damage in the notch-root. The a/W ratio set in this way varied between 0.05–0.6 and 0.05–0.5 for the Charpy and Izod specimens, respectively.

The specimens were subjected to instrumented impact bending without cushioning the striker at T = 20 and T = −40°C, respectively. Cooling down of the specimens occurred in a thermostatic chamber by evaporating liquid nitrogen. The instrumented impact pendulum (AFS-MK3 fractoscope of Ceast, Torino, Italy) records the force during impact as a function of time (F–t). The primary data stored can be converted into force–deflection (F–s), energy–time (E–t), and energy–deflection (E–s) traces as well. For the data storage and acquisition, a Hewlett-Packard computer (HP 9000) was used that was plugged to the above fractoscope and operated by a homemade data evaluation program. This program computed all necessary data by cursor movement at

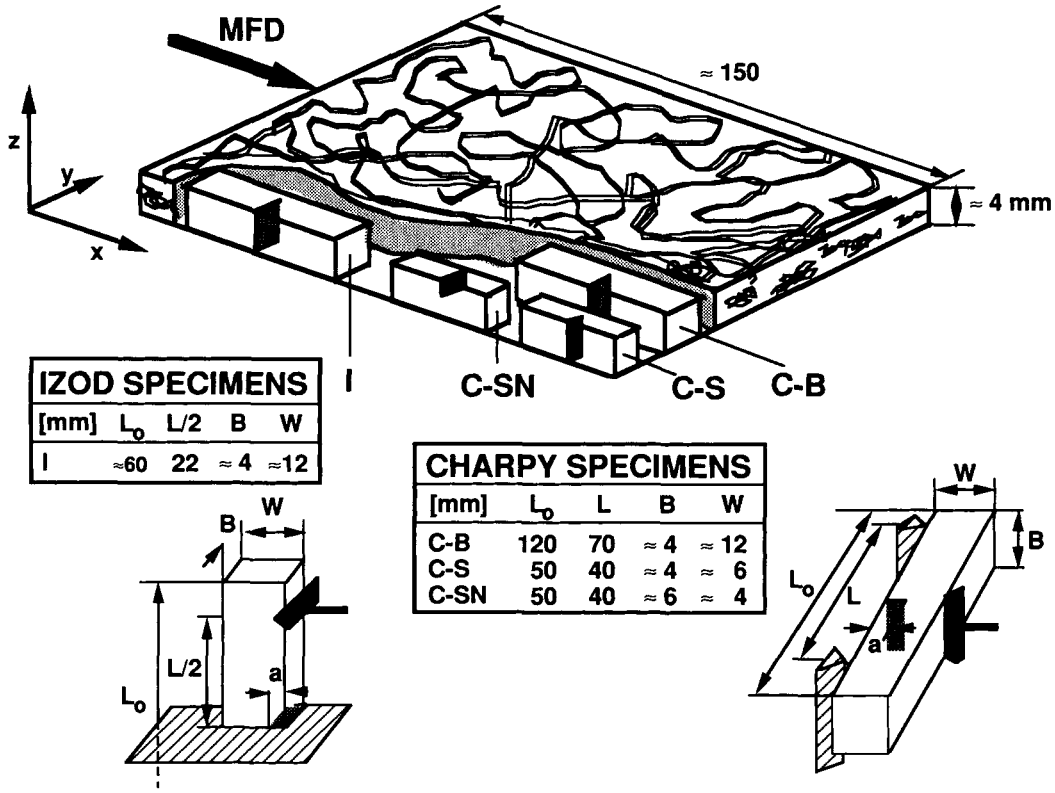

Figure 2 Machining, notching, designation, and dimension of the specimens used. MFD, mold-filling direction.

any displaying mode, from which F–s was preferred (cf. Fig. 3). Recording was undertaken at the following conditions:

	Charpy	Izod
Striker speed (m/s)	3.7	3.46
Striker energy (J)	15	7.5 and 25
Load range (N)	191–955	382–955
Sampling time (ms)	8–32	8–32

Analysis of Test Results

From the registered and computed data, the dynamic stress intensity factor or fracture toughness, K_d, the dynamic strain energy release rate or fracture energy, G_d, and the dynamic elastic modulus, E_d, were determined using eqs. (1), (2), and (3), respectively:

$$K_d = \sigma_{peak} \cdot Y \cdot a^{1/2} \quad (1a)$$

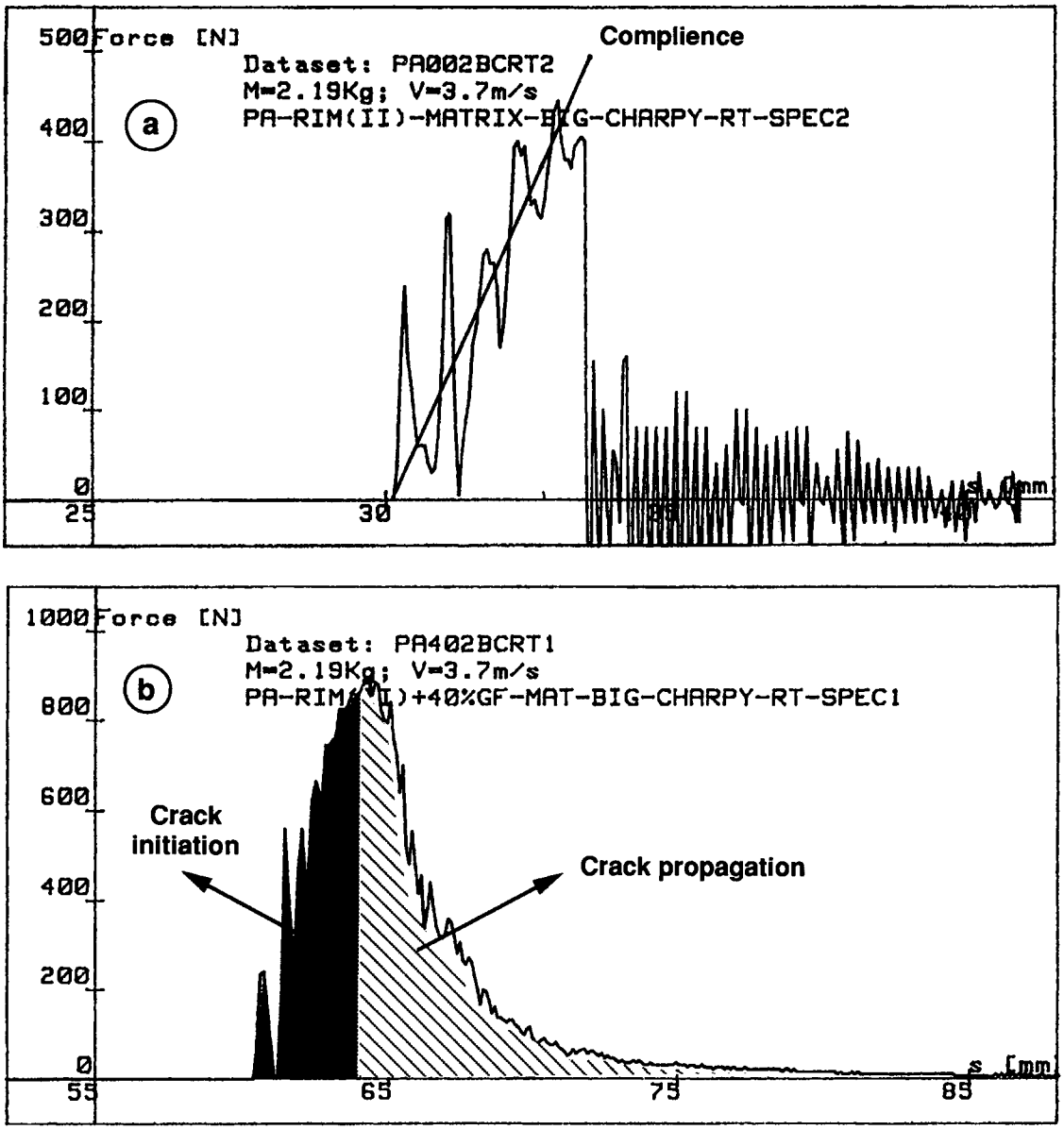

Figure 3 Characteristic load-displacement (F–s) fractograms for the (a) NBC-RIM matrix and (b) for its composite with 40 wt % GF mat reinforcement at T = 20°C on the example of C–B specimens (cf. Fig. 2). Determination of the compliance is shown in (a), whereas distinction between crack initiation and propagation is indicated in (b).

$$\sigma_{peak} = \frac{3 \cdot F_{peak} \cdot L}{2 \cdot B \cdot W^2} \text{ (Charpy)};$$

$$= \frac{6 \cdot F_{peak} \cdot L/2}{B \cdot W^2} \text{ (Izod)} \qquad (1b)$$

where σ_{peak} is the maximum stress; Y, the finite width correction factor[8]; a, the notch length, and F_{peak}, the maximum force (in brittle fracture) or the load that corresponds to the onset of crack propagation (in ductile fracture), and all other data are related to the specimen size (cf. Fig. 2). Since the Y factor is not yet known for the Izod specimens, the related Charpy correction values at $L/W = 6$ have been used. It was selected since the run of the Izod energy calibration factor, ϕ, as a function of a/W at $L/W = 4$ is very closely matched to the Charpy one at $L/W = 6$.[9] K_d was read from the slope of a straight line going through the origo and giving the best fit for the plot $\sigma \cdot Y$ vs. $a^{-1/2}$ according to eq. 1(a).

The energy absorbed up to the end of the crack initiation (E_{peak}; cf. Fig. 3) was considered to determine the initiation fracture energy, $G_{d,i}$, from

$$G_{d,i} = \frac{E_{peak}}{B \cdot W \cdot \phi} \qquad (2)$$

where ϕ is the energy calibration factor dependent on specimen type (Charpy, Izod), size, and notch dimensions (L/W and a/W ratios).[9,10] The total absorbed energy, E_{total}, to completely fracture the specimens could be determined only in a few cases (especially for the C–B specimens). The related fracture energy is designated as $G_{d,total}$.

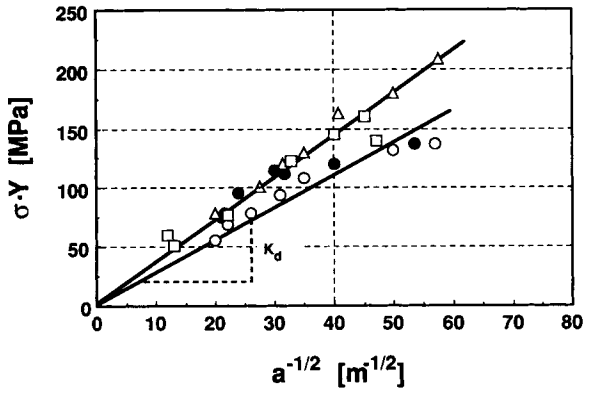

Figure 4 Evaluation of K_d of the NBC matrix at room temperature using high-speed impact bending test results of notched Izod and Charpy specimens of different dimensions: (△) Izod; (●) C–SN; (○) C–S; (□) C–B specimen.

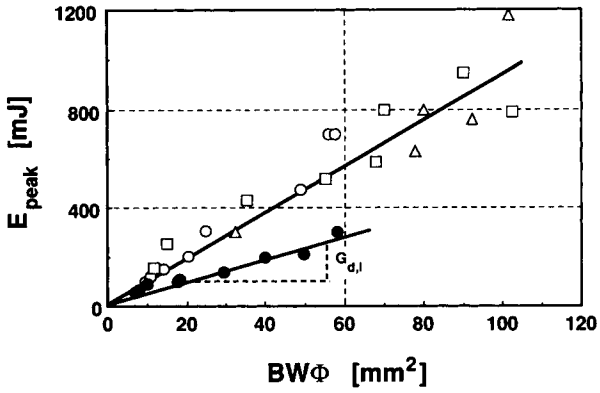

Figure 5 Determination of $G_{d,i}$ of the NBC matrix at room temperature using Izod and Charpy specimens of different types. For designations, see Figure 4.

The dynamic elastic modulus, E_d, was computed only for the Charpy specimens using the F–s traces[9]:

$$E_d = \frac{9 \cdot L^2}{2 \cdot B \cdot W^2} \cdot \frac{\phi_{(x)} \cdot Y^2_{(x)} \cdot x}{C_{(x)}} \qquad (3)$$

where $x = a/W$ and C is the compliance read as the slope of the F–s curve ($C = \Delta s/\Delta F$, cf. Fig. 3); the other parameters were explained before. Since all the measurements were performed in the crack opening mode (mode I), this index has been omitted from the fracture mechanics terms.

RESULTS AND DISCUSSION

Fracture and Failure Behavior of the Matrix

Effect of Specimen Type

Figure 4 illustrates that K_d does not depend on the size and type of the specimens. K_d values read from the related slopes of Figure 4 vary between 3.0 and 3.7 MPa $m^{1/2}$, i.e., they are within an acceptable experimental scatter.

Contrary to this, a very big scatter was observed in the initiation fracture energy, $G_{d,i}$. Although the lower and upper bounds of $G_{d,i}$ lie at 9.8 and 11 kJ/m^2, respectively (Fig. 5) for the C–S, C–B, and I specimens, only half of the above value was received using C–SN specimens. This was presumed to be a manifestation of an inherent microstructure of anisotropic character.[5] The existence of a molding-induced skin-core structure was evidenced, indeed, by polarized light microscopy (Fig. 6). The development of the core region showing flow contours can be explained by a plug-flow in the solidifying central

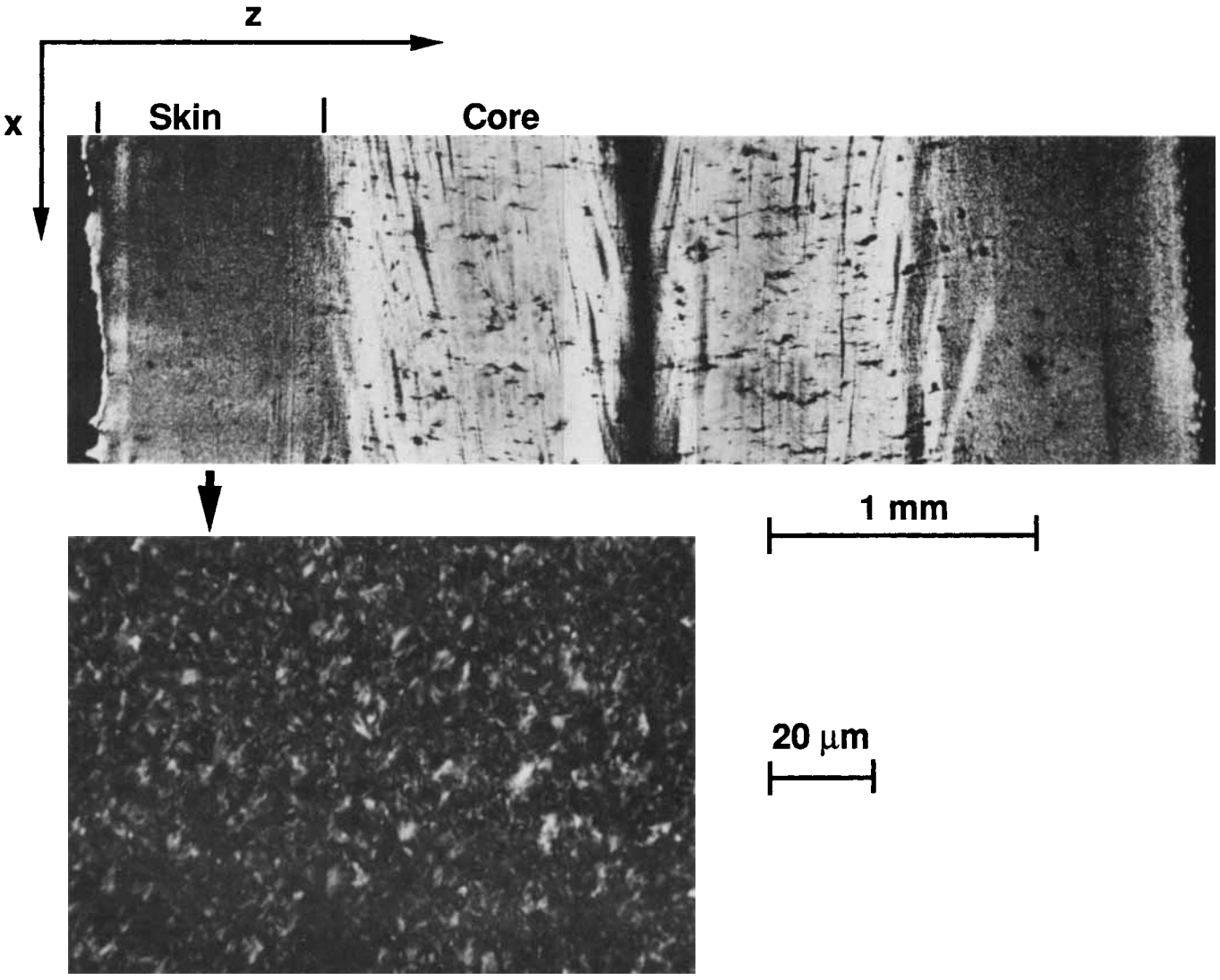

Figure 6 Light microscopic pictures taken on thin microtomed sections ($\approx$ 10 μm) of the NBC between crossed polarizers showing the molding-induced skin-core morphology. For designations, see Figure 2.

region due to the mold-filling pressure.[11] The bright band structure in the core is the consequence of a shear-induced crystallization process and therefore also implies an inner stress state. This type of crystallization was evidenced by the structural memory effect using a thermooptical method. This consists of a controlled melting and a subsequent recooling of thin polymer sections viewed in a light microscope between crossed polarizers.[12] The principle of this method is that the heat stability of the nuclei of various supermolecular formations is highly different so that the crystallization process can be "reconstructed" adequately upon recooling. Row nuclei generated by mechanical shear stresses are always more stable than those of isotropic spherulites,[13] which could be stated also in this case, verifying the aforementioned formation in the core. Analogous banded microstructures were reported for different polycondensates, including PAs.[11,14]

Deterioration in the fracture energy at C–SN notching (Fig. 5) can be attributed to a lower resistance of the core in this direction (z-axis) and/or to the missing upper skin layer with spherulitic structure due to the notching (cf. Figs. 2 and 6). It is well documented that characteristics of the spherulite texture (type and mean spherulite diameter, average crystallinity) may affect the fracture mechanics parameters considerably.[15,16]

The mean E_d values as an arithmetical average of the related ones calculated for each specimen by eq. (3) varied between 2.1 and 2.3 GPa. This range is very reasonable for this NBC formulation.[17]

The $G_{d,\text{total}}$ values determined according to eq. (2), using E_{total} instead of E_{peak}, agreed with the mean impact strength ($\bar{G}_d$), provided that values of completely failed specimens were considered. The mean impact strength was calculated by

$$\bar{G}_d = \frac{\sum_{i=1}^{n} \frac{E_{\text{total},i}}{B_i \cdot (W_i - a_i)}}{n} \tag{4}$$

The similar fracture energy values ($G_{d,\text{total}} \approx G_{d,i} \approx \bar{G}_d$) imply brittle fracture and thus the validity of the linear elastic fracture mechanics (LEFM).

Effect of Temperature

K_d values at −40°C do not differ much from those at RT, although the effect of specimen type turns out clearer. For the C–SN specimens, K_d = 2.8, whereas for all others, K_d = 3.8 MPa $m^{1/2}$ were deduced. For the former value, both the microstructure and the internal stress state, the effects of which becomes more affirmative at lower temperatures, are responsible.

Since K_d is practically constant and E_d slightly increases (E_d = 2.4–2.7 GPa) with a temperature decrease, $G_{d,i}$ should decrease following the approximation:

$$G_{d,i} = \frac{K_d^2}{E_d} \text{ (plane stress)} \tag{5}$$

which was, indeed, established. $G_{d,i}$ values were found between 4 and 7 kJ/m^2 at −40°C; the lower bound is again related to C–SN, whereas the upper one, to the other types of specimens. Inserting the K_d and E_d values reported above, eq. (5) yields highly reliable results, especially at −40°C.

The effect of the specimen geometry on the fracture behavior becomes more obvious considering the ductility index (DI)[3]:

$$DI = \frac{E_{\text{total}} - E_{\text{peak}}}{E_{\text{total}}} \tag{6}$$

which is related to the relative proportion of the crack propagation and, thus, to ductile failure manner. The closer DI is to 0, the more pronounced is the brittle fracture, whereas increasing DI (up to 1) corresponds to an intensification in ductile failure.

Average DI values for the I, C–S, C–SN, and C–B specimens at RT and at different a/W ratios were found at ≈ 0.7, 0.6, 0.4, and 0.1, respectively. These values decreased steeply at −40°C ($DI \approx$ 0.06–0.08) and the dependence on specimen type disappeared. It should be noted here that not all specimens separated completely at RT. This fact combined with the related DI values imply the importance of the relation of the span to that of the full length of the specimens (cf. Fig. 2) for materials of high impact toughness and, thus, of high bending ability.

In addition, it was demonstrated that NBC tends to undergo crack tip blunting,[17] which should be influenced by both the stress state of the specimen (cantilever or three-point bending) upon loading and by possible microstructural transitions in the notch tip due to the suddenly introduced mechanical work. A stretched zone of about 0.1 mm width at the razor notch evidences for such crack tip blunting (Fig. 7). The rather big scatter observed in DI at RT, mostly as a function of a/W, for the same type of specimens may pertain to this stress state and to related microstructural alterations (e.g., promoted by local adiabatic heating) during impact.

The above effects may result in the formation of a "plastic hinge" that holds the sides of the specimen together. The reason why the molding-induced microstructure is not reflected in Figure 7 can be ascribed to a special failure mode "desmearing" the initial texture. Secondary cracks initiated at undissolved catalyst rests according to energy-dispersive X-ray analysis[18] (designated as C in Fig. 7) interfere with the main crack and thus depress the effects of the initial morphology, especially at ambient temperature.

The different DI values of the C–S and C–SN specimens are of importance. The lower DI value of C–SN suggests a lower resistance to fracture due to the microstructural buildup detected.

Fracture and Failure Behavior of the Composites

Effect of Specimen Type

Figure 8 makes obvious that the specimen type, more exactly the ligament width (W), highly affects the K_d values of these swirl mat-reinforced composites. $K_d \approx$ 5 MPa $m^{1/2}$ was determined for the small Charpy specimens (C–S, C–SN), whereas $K_d \approx$ 7.5 MPa $m^{1/2}$ was found for the I and C–B specimens of the same ligament width. The main reason for it was that the C–S and C–SN specimens underwent bending in impact and, thus, by becoming shorter than the span length, flew through the jig without

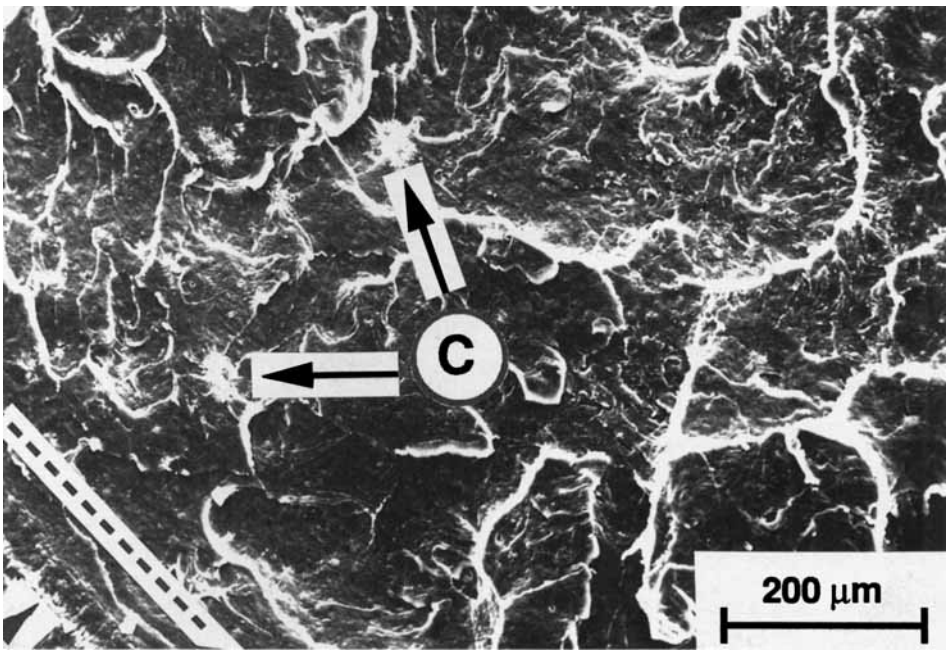

Figure 7 SEM picture showing a stretched zone (indicated by broken line) next to the razor blade notch (arrow) due to crack tip blunting on the example of an Izod specimen fractured at RT. "Dimple" fracture surface of the NBC is due to a microductile deformation of the matrix. In the cracterlike spots, undissolved parts of the RIM catalyst (C) can be evidenced by energy-dispersive analysis of X-rays.[18]

total separation (Fig. 9). Figure 9 demonstrates also very clearly that now the separation of the specimen is impeded by a "hinge" effect of the deformed and partially destroyed GF mat. The load-bearing capacity of this hinge in the bending mode is very low,

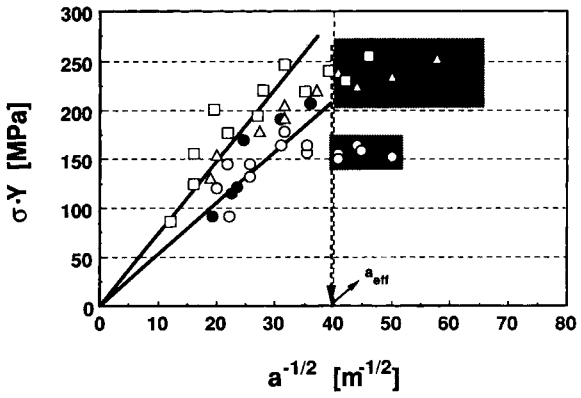

Figure 8 Evaluation of K_d using Izod and Charpy specimens of different types on the example of the 25 wt % GF mat-reinforced NBC at room temperature. Data of specimens showing failure away from the notch are within the shadowed area; denoting of specimens is according to Figure 4.

being in a range of 1/20–1/50 of the related F_{peak} for the different specimens in function of their initial a/W value. This is closely matched to the scatter range in the F_{peak} due to the local arrangement of the mat; therefore, the determination of K_d by eq. (1) is practically unaffected by the fact that the specimen is not fully separated. Data included in the shadowed field in Figure 8 are omitted from the evaluation since their failure did not occur at the notch. This can be seen in Figure 9, showing that the failure site is away from the notch marked by ink. It means that there is a lower threshold of the "effective" notch depth (a_{eff}). Its value is between 0.5 and 0.6 mm for the 25% GF mat-reinforced NBC based on the onset of failure away from the notch (calculated by considering the left-side value of the shadowed range in Fig. 8). This threshold value should be taken into consideration when calculating K_d. The I specimens were not separated either, but it was practically the case for the C–B specimens possessing the highest length-to-span ratio (120 to 70 mm; cf. Fig. 2).

Analogous changes with respect to the specimen type were also detected in the run of the $G_{d,i}$ values (Fig. 10). $G_{d,i}$ = 16 kJ/m^2 was received for the C–S and C–SN, and $\approx$ 24 kJ/m^2 was read from the

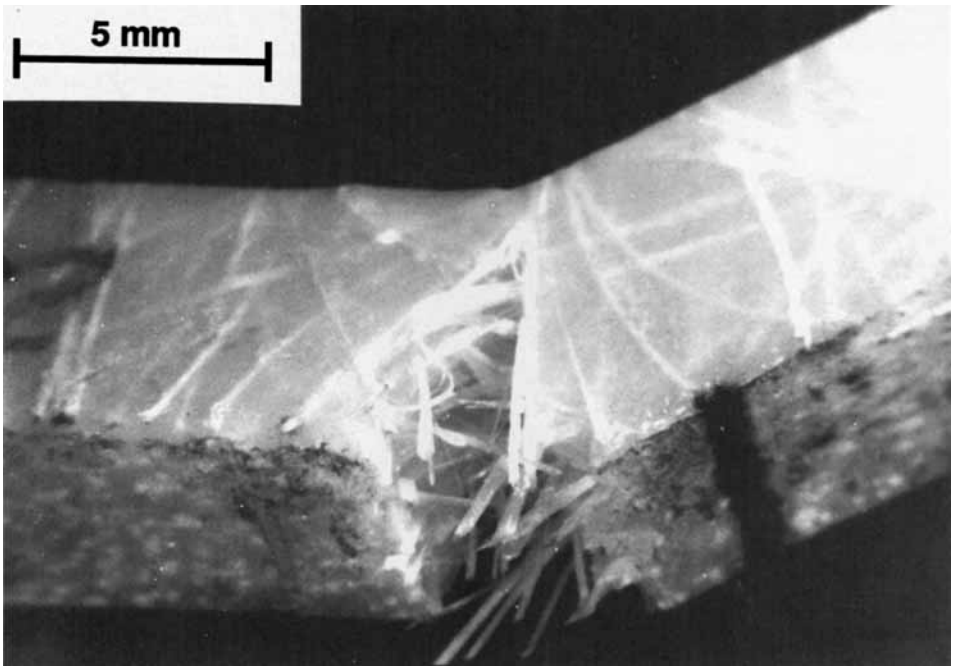

Figure 9 Macrophotograph taken from an impacted C–S specimen of NBC with 25 wt % GF mat. This figure illustrates that the failure site is away from the razor blade notch marked by ink; initial razor notch depth, 0.4 mm ($a/W = 0.07$).

related slopes in Figure 10 for the I and C–B specimens. The above findings underline that fracture mechanics values may be considerably underestimated when specimens of inadequate dimensions are used.

The E_{peak}–$BW\Phi$ functions given in Figure 10 allow again the detection of a specimen-related maximum flaw size that corresponds to the a_{eff}. From the critical $BW\Phi$ value, separating the valid and invalid data pairs (letters in the shadowed area in Fig. 10), Φ can be calculated. With Φ being a function of a/W (Refs. 9 and 10) permits the estimation of a_{eff}. For the I and C–B specimens, a_{eff} was found to be between 0.5 and 0.7 mm, in good agreement with the related value deduced from the plot of K_d calculation (cf. Fig. 8). On the other hand, this value is underestimated ($\approx$ 0.3 mm) again for the C–S specimens of a similar type of notching. The knowledge of a_{eff} is very useful not only from the point of view of fracture mechanical evaluation but also from that of quality detection and assurance. For its determination, the G_d plot seems to be more adequate than the K_d, since the correction factor Φ changes very steeply at low a/W values.[9,10,19] a_{eff} derived from results achieved on I and C–B specimens is connected mostly with a machining-induced flaw size,[19] although other effects (e.g., local arrangement of the swirl mat resulting in weak sites, imperfect wetting of the GF strand by the matrix) are also involved. Sawing, used in our case, dislodges and splits the strands. The long-range debonding of rovings being caused in this way. This was evidenced, in fact, by ink penetration. Provided that sawing generates flaws, their average size should increase with the fiber volume fraction (V_f) due to a hindered matrix damping. Figure 11 shows that a_{eff} increased from

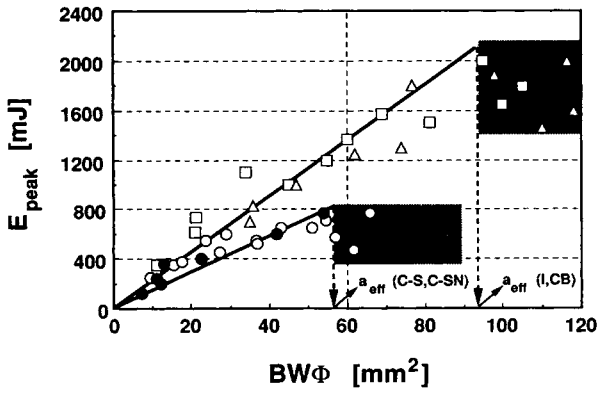

Figure 10 Determination of $G_{d,i}$ for the composite with 25 wt % GF swirl mat at room temperature using Izod and Charpy specimens of different types. For designations, see Figures 4 and 8.

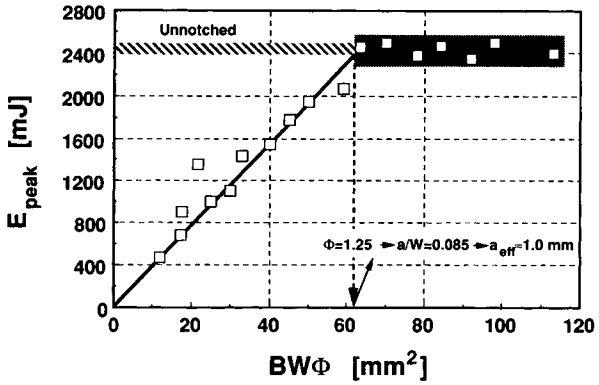

Figure 11 Determination of $G_{d,i}$ and a_{eff} for the composite with 40 wt % GF swirl mat at room temperature using C–B data. For designations, see Figures 4 and 8.

0.7 mm (cf. Fig. 10) to 1.0 mm for C–B specimens by increasing the GF mat content from 25 to 40 wt % ($V_f \approx 0.12$ and 0.22, respectively). Figure 11 also shows that the data pairs related to the failure of the specimens away from the notch are within a small scatter range, which agrees, additionally, with the level of the unnotched specimens. It is because arrangement of the GF mat in the microscopic level becomes more and more uniform with increasing V_f (compare the scatter ranges of the data omitted from the calculation in Figs. 10 and 11). The intersection of the E_{peak} of the unnotched specimens with that of the regression line fitted for the data pairs can also be used for the determination of fiber-induced notch-rising.[19] a_{eff} derived from the C–SN or analogously notched specimens, on the other hand, provides information about the surface quality of the molded part.[5] a_{eff} proved to be 0.3 mm in this case. This value is very closely matched to the mean size of "surface flaws" caused by air bubbles entrapped in the mold during processing (Fig. 12).

Effect of Temperature

The effect of specimen size on the fracture mechanics values tends to decrease or even diminish with decreasing temperature. K_d of the 25 wt % GF mat-reinforced NBC varied between 7.5 (C–SN) and 9 MPa $m^{1/2}$ (I, C–B), whereas $G_{d,i}$ seemed to be independent of specimen type (≈ 30 kJ/m^2) according to Figure 13. This is because the requirements of the LEFM are better fulfilled at lower temperatures.

Decreasing temperature resulted in a slight increase of a_{eff}. Provided that the threshold $BW\Phi \approx 70$ mm^2 for the I and C–B specimens [cf. Fig. 13(b)], a_{eff} values between 0.8 and 0.9 mm can be deduced. This may be an effect of additional notch rising due

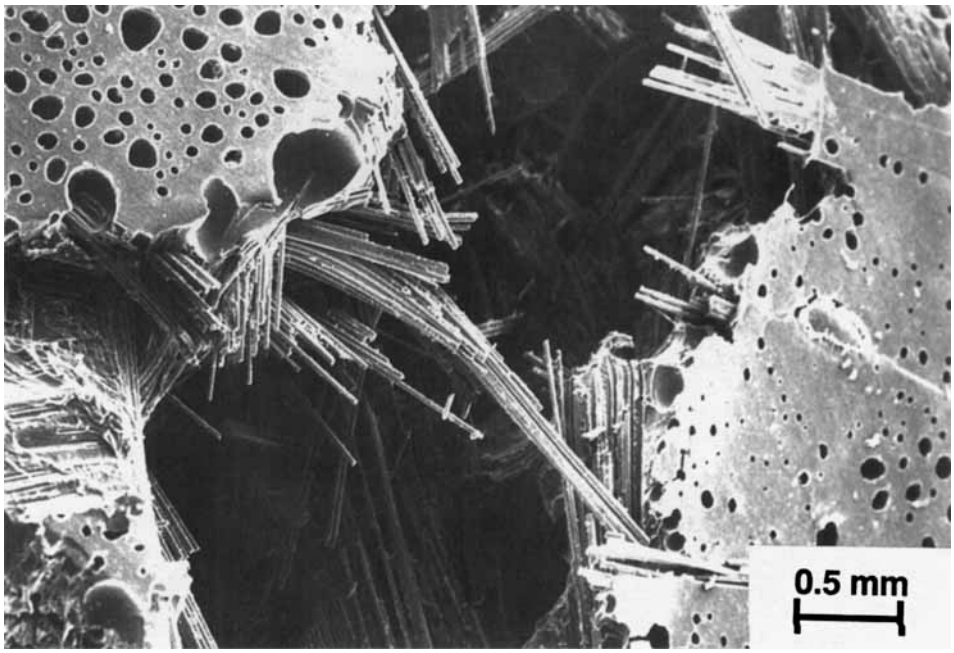

Figure 12 SEM picture taken from an unnotched C–SN specimen of NBC with 50 wt % GF mat reinforcement. Craters due to "air" bubbles are clearly perceptible on the surface. In their origin, several effects may be included: inadequate venting of the mold, pronounced air adsorption by the mat, dissolution of the blanking N_2 in the RIM component, etc.

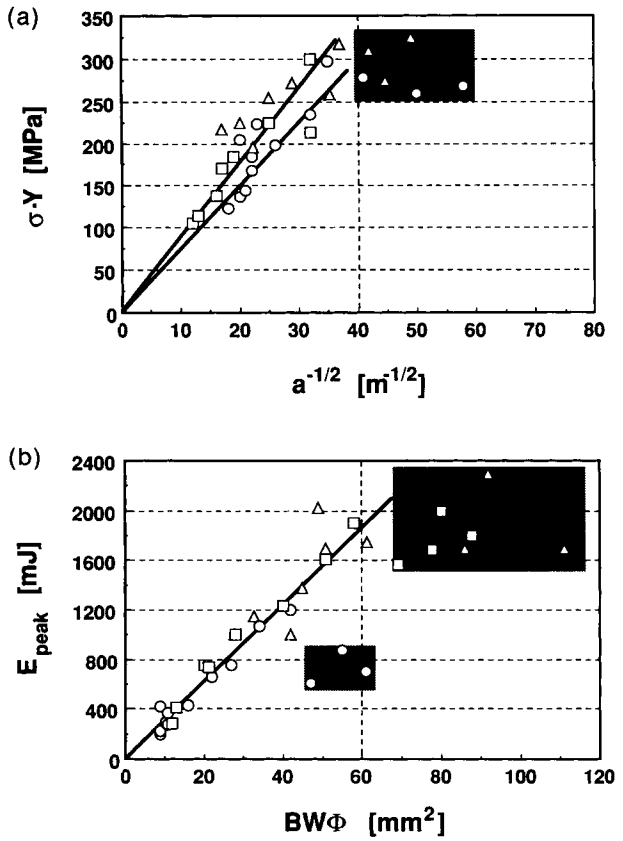

Figure 13 (a) Evaluation of K_d value for the NBC with 25 wt % GF mat at $T = -40°C$ using Izod and Charpy specimens of different types. (b) Evaluation of $G_{d,i}$ value for the NBC with 25 wt % GF mat at $T = -40°C$ using Izod and Charpy specimens of different types. For designations, see Figures 4 and 8.

to differences in the thermal expansion coefficients between the matrix and GF as well as that of water sorption and, thus, of ice formation. a_{eff} was again strongly underestimated for the C–S specimens (≈ 0.5 mm).

Complete separation of the specimens was observed only for the C–B and C–S specimens. This fact suggests that the in-plane and out-of-plane network deformability of the GF strand mat incorporated into the NBC matrix is different. The latter occurs at lower loads when comparing C–S and C–SN results, as could be expected. It is believed that alterations in *DI* indicate implicitly for this network-, mesh-type deformation (see later).

Decreasing temperature increases E_d of the 25 wt % GF mat-reinforced NBC from 2.9 to 3.4 GPa. $G_{d,i}$ calculated by eq. (5) using the above K_d and E_d values agreed well with that read from the plot in Figure 13(b) for the C–B specimens.

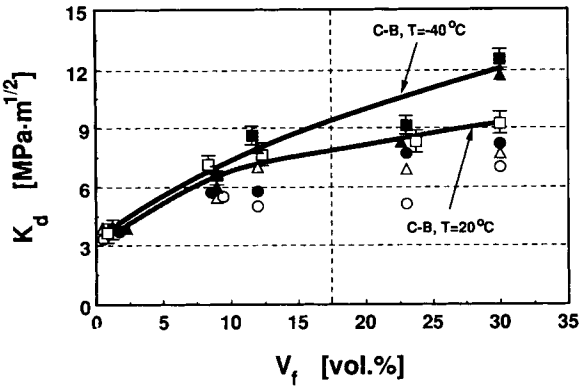

Figure 14 Run of K_d in function of V_f and temperature for the specimens of analogous notching (I, C–S, C–B). Designations: see Figure 4; open symbols relate to results at T = RT; filled ones, at $T = -40°C$.

Effect of Fiber Volume Faction

The runs of K_d and $G_{d,i}$ as a function of V_f and T are given for the specimens of analogous notching in Figures 14 and 15, respectively. From the point of view of the highest fracture mechanics values, the following ranking of the specimens can be concluded:

$$\text{C–SN} < \text{C–S} < \text{I} < \text{C–B}$$

which fully agrees with the change in the ligament width. Based on the ligament width, on the other hand, no distinction between I and C–B was anticipated. Alterations in the related data are probably caused by a difference in the stress state in cantilever and three-point impact bending and by the effect of length-to-span ratio of the specimens. Based on the above ranking, one can conclude that reliable fracture mechanics values for GF swirl mat-reinforced

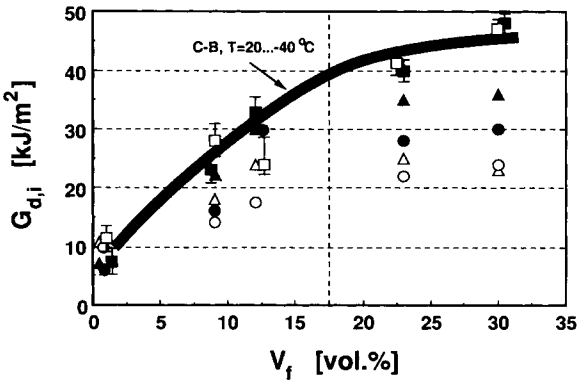

Figure 15 Run of $G_{d,i}$ in function of V_f and temperature for the specimens of analogous notching (I, C–S, C–B). For designations, see Figure 14.

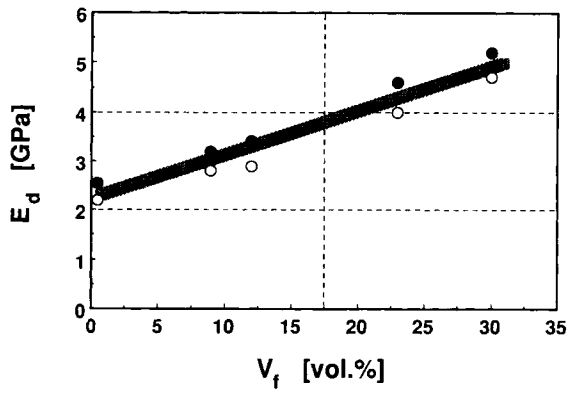

Figure 16 Run of E_d as a function of V_f and temperature for the GF swirl mat-reinforced NBC composites. E_d is the average value for the I, C–S, and C–B specimens. For designation, cf. Figure 14.

composites can be achieved only when the specimen size, more exactly the ligament width, is properly chosen ($W > 12$ mm in this case). Note that the width of the coupons used in the works of Stokes[6,20] in order to determine the tensile characteristics of GF mat-reinforced polypropylene was exactly 12.7 mm (= 0.5 in.).

The $G_{d,i}$ values are below the related ones published for GF mat-reinforced PA-6 RIM[3] but far beyond to those of hammer-milled GF-filled NBC[17] or chopped GF-reinforced systems. The latter fact cannot be merely attributed to an effect of fiber aspect ratio (l/d). The estimated range of l/d in the GF mat-reinforced composites is between 50 and 80, considering the ligament width (W) and mean strand diameter, which agrees with that of chopped GF but lies higher than hammer-milled GF ($l/d \approx 5$–10).[21] Therefore, it is obvious that the network buildup of the GF mat shown in Figure 1 cannot be neglected. Incorporation of the GF mat is accompanied with the development of additional new energy dissipating mechanisms. The reason why $G_{d,i}$ is about half of the published value for PA-6 RIM[3] is not clear at all. Since the NBC is tougher than the unmodified PA-6 used in Ref. 3, an upgrading in $G_{d,i}$ was presumed in our case. The opposite trend may be connected with interface bonding and related failure phenomena.

K_d increases slightly, while $G_{d,i}$ does not hardly change with decreasing temperature, as illustrated in Figures 14 and 15 for the C–S, C–B, and I specimens of analogous notching. This confirms that NBC with GF swirl mat reinforcement exhibits a well-balanced stiffness/toughness property profile over a broad temperature range that is of paramount interest for materials in automotive applications. The saturation-type course of the $G_{d,i}$ vs. the V_f curve (cf. Fig. 15) can be explained by eq. (5): The effect of a slight increment in K_d (cf. Fig. 14) is averaged out by a pronounced increase in E_d (cf. Fig. 16).

The run of E_d as a function of V_f and temperature is given in Figure 16. E_d increases monotonously with increasing V_f, as expected. Mapping of the fracture mechanics values (K_d, $G_{d,i}$, and E_d) as a function of GF mat content and testing variables (temperature, impact speed, or fracture frequency) seems to be a very useful tool for design and construction. Such a fracture map, the construction of which requires further work, may deliver information about both stiffness and toughness characteristics of the material at different testing and, thus, service conditions.

Effect of GF Mat Type

As reported before, investigations were carried out also on composites reinforced by the same amount of GF mat with the same basic characteristics but containing also stronger filaments (B mat). The results listed in Table I indicate that incorporation of GF mat with stronger constituting filaments is beneficial for the fracture properties. This should be related, in fact, to some modifications in the failure events during impact.

Table I Comparison of the Results of NBC Matrix Composites with 18 wt % GF Mat (V_f = 8.9 vol %) Composed of Filaments of Different Strength

	C–B Specimen				I Specimen			
	K_d (MPa m$^{1/2}$)		$G_{d,i}$ (kJ/m^2)		K_d (MPa m$^{1/2}$)		$G_{d,i}$ (kJ/m^2)	
GF Mat	−40°C	20°C	−40°C	20°C	−40°C	20°C	−40°C	20°C
A	5.3	4.7	15.0	13.0	5.1	4.7	12.1	11.8
B	7.5	6.0	25.1	19.4	7.1	5.5	22.1	17.7

A, mat built-up of the same GF filaments of lower strength; B, mat containing mixed filaments both of lower and higher strength.

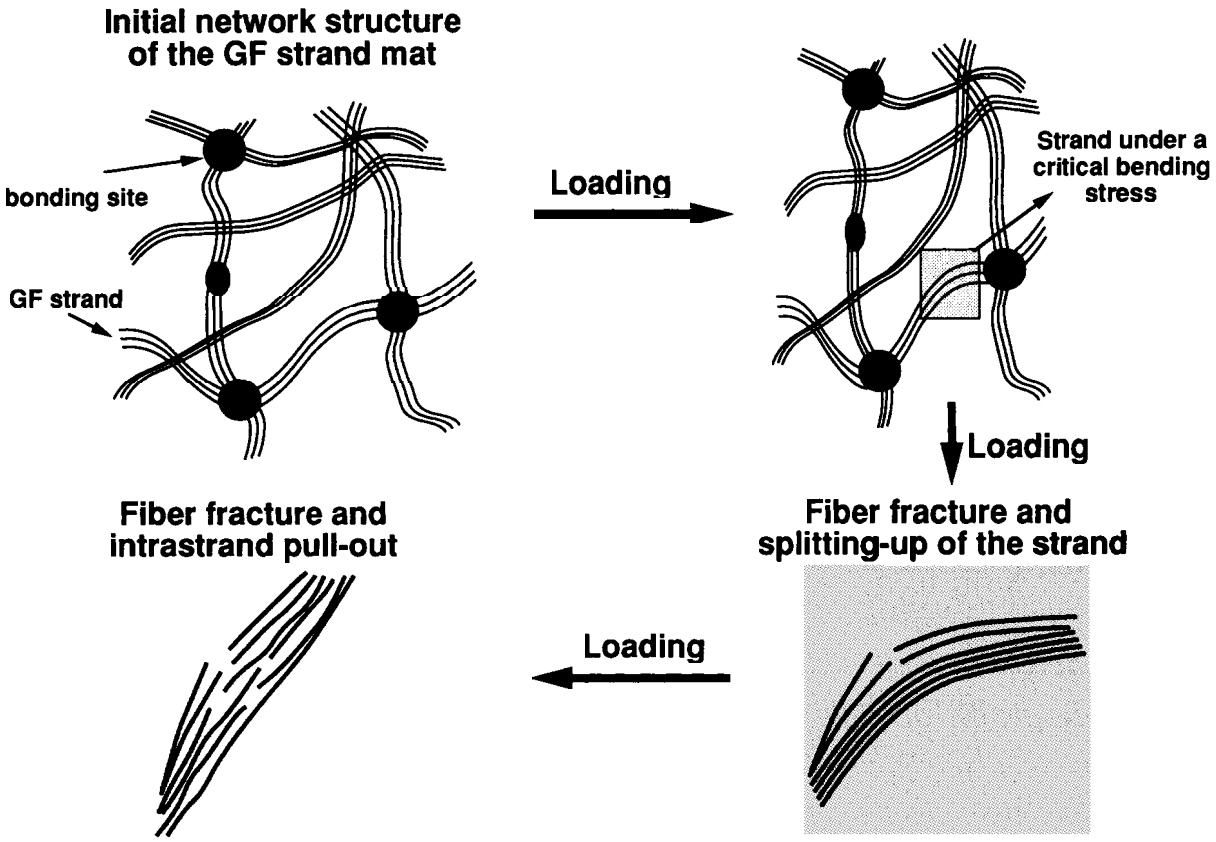

Figure 17 Failure sequence of the GF strand mat in a tough matrix, schematically.

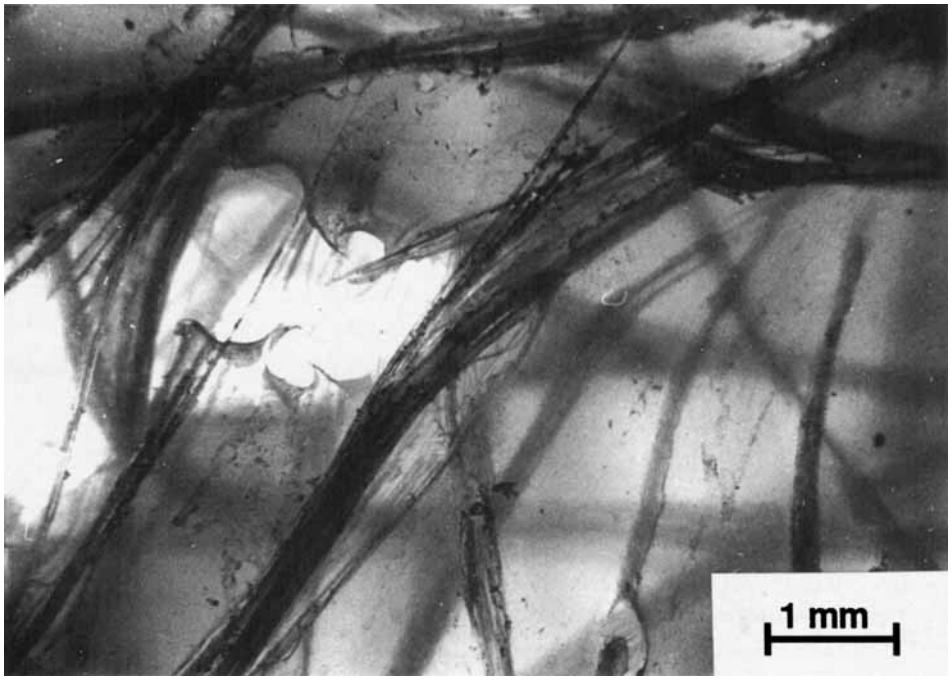

Figure 18 Breakage of the GF strands upon bending stresses in static fracture test of an NBC composite with 25 wt % GF mat. Brightfield photograph taken during tensile loading of a compact tension specimen at RT and 1 mm/min crosshead speed.

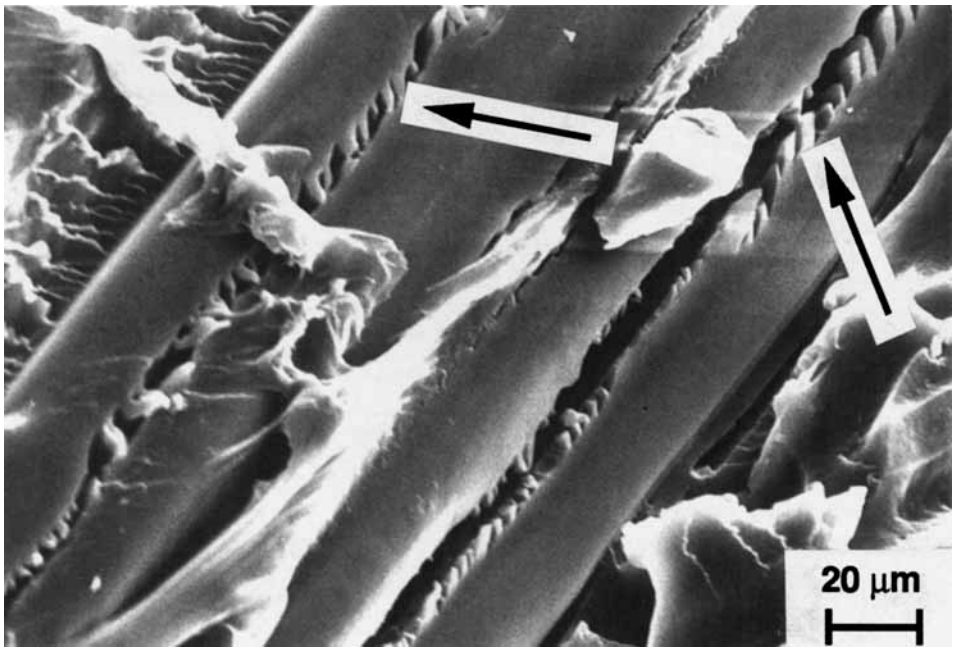

Figure 19 Shear deformation of the matrix at the GF interface caused by pullout of the strand and its constituting filaments. Arrows indicate for sites of shear hackling.

Failure Behavior

It is well known that fiber debonding, pullout, and breakage constitute the fiber-related failure events in traditional short-fiber-reinforced plastics having an l/d ratio below ca. 80.[22] These processes were extended with fiber bridging for longer-fiber-reinforced systems ($l/d > 500$). For the GF mat-reinforced systems, a further specification seems to be necessary: a network or mesh-type deformation and subsequent failure of the mat (cf. Fig. 17). This was the reason why specimens did not always separate totally (cf. Fig. 9). Obviously, this kind of deformation strongly depends both on the mesh size of the mat (set by "gluing," bonding the strands, cf. Fig. 1) and on the ductility of the matrix. It is therefore recommended to "tailor" the mat characteristics to those of the matrix in order to get synergism in energy absorption. As shown schematically in Figure 17, the next step after network deformation is the breaking up of the strands due to bending stresses created by loading. This was evidenced in low-speed static fracture tests[23] and is shown in Figure 18. The following steps are pullout processes among individual and/or bunched filaments within the strands as well as their "slippage" along the fiber/matrix interface (Fig. 19). In Figure 19, shear hackles along the GF reveals the latter process. This underlines the importance of a proper sizing of the fibers also within the roving.

To the above fiber-related new energy absorption mechanisms, changes in the related matrix deformation should be accounted for in order to explain the observed increase in $G_{d,i}$. The processing zone in this case is much broader due to the network structure of the mat than for chopped fiber-reinforced systems. The saturation-type run of $G_{d,i}$ vs. V_f (Fig. 15) or DI vs. V_f (Fig. 20) indicates that a loss in the energy consumption due to hindered matrix deformation at higher V_f is compensated by rising fiber-related energy-dissipation events. The rel-

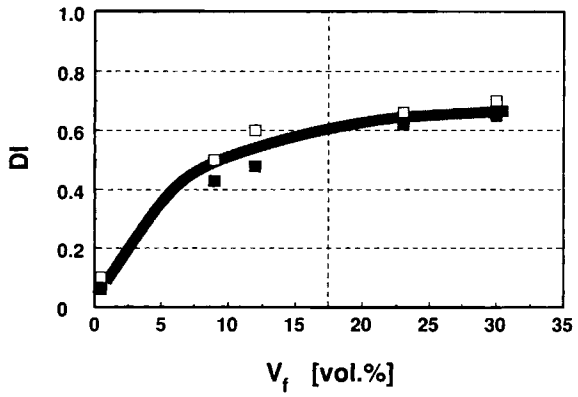

Figure 20 Change in DI within the a/W range of 0.2–0.3 as a function of V_f and temperature for the C–B specimens. Open symbols relate to results at T = RT; filled ones, at $T = -40°C$.

ative proportion of them, on the other hand, should change with V_f, e.g., instead of mesh-type deformation, strand breakage and fiber fracture dominate at higher V_f. *DI* values of the C–B specimens plotted against V_f and temperature demonstrate how GF mat improves (at RT) or generates (at $T = -40°C$) crack propagation in the NBC, which is a process of high-energy consumption. In this crack propagation process, the above failure events are, in fact, involved. The run of *DI* vs. V_f at RT is practically identical with that of PA-6 RIM reinforced with GF mat.[3]

CONCLUSIONS

This study performed on the fracture mechanical characterization of a continuous glass strand mat-reinforced reaction injection-molded (RIM) polyamide block copolymer (NBC) at instrumented high-speed impact bending has led to the following conclusions:

1. The fracture mechanics data depend greatly on the specimen type (including the notching direction) and size—more exactly, on the ligament width (W) and on the length to span ratio (L_0/L). For such systems, choosing of $W > 12$ mm and $L_0/L > 1.7$ seems to be adequate.
2. Differences in the fracture energy of the matrix were caused by a molding-induced anisotropic morphology.
3. The fracture toughness of the composites increased, whereas the fracture energy seemed to reach a plateau in function of fiber mat content when specimens of proper size were considered. These fracture mechanics parameters were only slightly affected by the temperature.
4. Use of the impact data supported by the observation of the failure site can be served for estimation of a machining- and molding-induced flaw size. The sawing-induced latent notch size was found between 0.6 and 1.0 mm, whereas the molding-induced one due to air bubbles was at about 0.3 mm.
5. New failure events were evidenced for the GF mat-reinforced composites, and the run of the fracture mechanics data as a function of reinforcement content was disputed by them. Incorporation of GF mat promotes crack propagation mostly due to its network deformation that can be treated as a special crack tip blunting process in the tough NBC matrix.

The financial support of this study by the EURAM program of the European Community (MA 1E/0043/C) is gratefully acknowledged.

REFERENCES

1. R. M. Hedrick, J. D. Gabbert, and M. H. Wohl, in *Reaction Injection Molding,* (ACS Symp. Ser. 270), American Chemical Society, Washington, DC, 1985, p. 135.
2. J. D. Gabbert, A. Y. Gardner, and R. M. Hedrick, *Polym. Compos.*, **4,** 196 (1983).
3. J. U. Otaigbe and W. G. Harland, *J. Appl. Polym. Sci.*, **37,** 77 (1989).
4. C. W. Knakal and D. R. Ireland, Instrumented dart impact evaluation of some automotive plastics and composites. ASTM STP 936, S. L. Kessler, G. C. Adams, S. B. Driscoll, and D. R. Ireland, Eds., Am. Soc. Test. Mater., Philadelphia, 1987, p. 44.
5. J. Karger-Kocsis, *Polym. Bull.*, **24,** 341 (1990).
6. V. K. Stokes, *Polym. Compos.*, **11,** 32 (1990).
7. B. Wunderlich, *Macromolecular Physics, Crystal Melting,* Academic Press, New York, 1980, p. 71.
8. W. F. Brown and J. E. Srawley, Plane strain crack toughness testing of high strength metallic materials. ASTM STP 410, Am. Soc. Test. Mater., Philadelphia, 1966, p. 3.
9. J. G. Williams, *Fracture Mechanics of Polymers,* Ellis Horwood, Chichester, 1984.
10. E. Plati and J. G. Williams, *Polym. Eng. Sci.*, **15,** 470 (1975).
11. J. E. Callear and J. B. Shortall, *J. Mater. Sci.*, **12,** 141 (1977).
12. J. Varga, *Period. Polytechn. Chem. Eng.*, **28,** 117 (1984).
13. J. Varga, *Angew. Makromol. Chem.*, **112,** 191 (1983).
14. J. Karger-Kocsis and K. Friedrich, *Plast. Rubb. Process. Appl.*, **12,** 63 (1989).
15. K. Friedrich, in *Advances in Polymer Science 52/53,* H. H. Kausch, Ed., Springer, Berlin, 1983, p. 225.
16. J. Karger-Kocsis, *Composites,* **21,** 243 (1990).
17. J. Karger-Kocsis, J. Daugaard, and L. Amby, *J. Polym. Eng.*, in press.
18. J. Karger-Kocsis, in *International Encyclopedia of Composites,* Vol. 5, S. M. Lee, Ed., VCH, New York, 1991, p. 337.
19. M. Akay and D. Barkley, *Polym. Test.*, **7,** 391 (1987).
20. V. K. Stokes, *Polym. Compos.*, **11,** 354 (1990).
21. C. W. Macosko, *RIM, Fundamentals of Reaction Injection Molding,* Hanser, Munich, 1989, p. 212.
22. K. Friedrich, in *Application of Fracture Mechanics to Composite Materials,* K. Friedrich, Ed., Elsevier, Amsterdam, 1989, Chap. 11, p. 425.
23. J. Karger-Kocsis and K. Friedrich, in *Durability of Polymer Based Composite Systems for Structural Applications,* A. H. Cardon and G. Verchery, Eds., Elsevier, London, 1991, p. 158.

Received February 25, 1991
Accepted October 10, 1991